AAS 25-157

FLEXIBLE MANEUVER PLANNING FOR COLLISION AVOIDANCE IN L_1/L_2 LIBRATION POINT ORBITS

Lorin Nugent,* Kathleen Howell,† and Diane Davis‡

Collision avoidance in cislunar libration point orbits presents challenges due to the highly sensitive dynamical environment. This investigation builds on previous work leveraging stretching and restoring directions as a basis for relative trajectory design, relying exclusively on information available via the state transition matrix. A strategy is developed to uncover impulsive maneuvers resulting in diverted arcs that successfully avoid a hazardous space object and then naturally return toward the reference orbit. The methodology is evaluated across sample libration point orbits in the circular restricted three-body problem, in addition to a preliminary assessments along trajectories in a higher-fidelity ephemeris model.

INTRODUCTION

As the number of missions to the lunar vicinity increases, so does the risk of collisions between objects. There is a proliferation of space debris in Earth orbit, due in part to impacts between human-made objects. As of 2022, the International Space Station maneuvers to mitigate the likelihood of collision with hazardous debris over once per year on average.[1] In a low-Earth orbital environment, the effects of a maneuver are well-understood – a small velocity change in an elliptical orbit results in another slightly modified elliptical orbit. In the chaotic environment of cislunar space, particularly for libration point orbits, small maneuvers may result in very different dynamical behavior depending on the direction, magnitude, and location of the maneuver. The NASA Gateway space station is planned to operate in a Near Rectilinear Halo Orbit (NRHO), an L_2 libration point orbit that periodically passes close to the lunar north pole.[2] The baseline orbit for Gateway must be appropriately maintained to avoid eclipses and to preserve phasing for visiting vehicles. The pairing of sensitive dynamics within the cislunar environment and strict orbit requirements offers challenges for efficient maneuver planning for collision avoidance.

Collision avoidance maneuver (CAM) design is a broad field with particular relevance in the concentrated near-Earth environment. Related studies focus on determining fuel-optimal control inputs to minimize collision probability with varying propulsion types,[3,4] as well as automating the process for on-board computation capabilities.[5] While the most pressing need for collision avoidance exists near Earth, some attention has been given to cislunar applications. De Maria et al. extend CAM optimization techniques typically leveraged in a two-body environment to Earth-Moon L_1 NRHOs.[6] More recently, Pavanello et al. approach CAM design using a recursive polynomial method as a function of the control input, providing a sample evaluation on an L_1 NRHO.[7] While much development in CAM design focuses on optimization techniques, Davis et al. offer a dynamical perspective for maneuver design, completing a preliminary investigation for Gateway operations.[8] The authors leverage the most restoring direction as determined from a linear analysis to define the maneuver direction, with downstream variations absorbed by routine stationkeeping operations. This approach is demonstrated to be effective for avoidance but identifies only a single maneuver option. Stretching and restoring directions are also applied more generally for applications to relative trajectory design near cislunar orbits.[9] The current investigation applies this general formulation to determine CAM options subject to constraints on the resulting trajectory diversion characteristics.

*Graduate Student, School of Aeronautics and Astronautics, Purdue University, West Lafayette, IN; nugentl@purdue.edu.
†Hsu Lo Distinguished Professor, School of Aeronautics and Astronautics, Purdue University, West Lafayette, IN; howell@purdue.edu.
‡Gateway Mission Design Lead, Johnson Space Center, Houston TX; diane.c.davis@nasa.gov.

DYNAMICAL MODELS

Two dynamical models are employed to simulate spacecraft behavior in the Earth-Moon system. A majority of analysis occurs in the circular restricted three-body problem (CR3BP), then sample results are demonstrated in a higher-fidelity ephemeris model (HFEM). This section provides a high-level overview of each of the two models.

The Circular Restricted Three-Body Problem

In the CR3BP, the mass of a spacecraft P_3 is infinitesimal compared to the masses of the primary bodies, P_1 (the larger primary, i.e., Earth) and P_2 (the smaller primary, i.e., Moon). The primaries, therefore, exist as an isolated two-body system, orbiting their mutual barycenter on closed conics, assumed circular. A rotating coordinate frame is defined with an origin at the barycenter such that $\hat{x}$ is always directed from P_1 to P_2, $\hat{z}$ is aligned parallel to the direction of the orbital angular momentum for the primaries, and $\hat{y} = \hat{z} \times \hat{x}$. The nondimensional position and velocity components form the full six-dimensional state vector of the particle P_3, i.e., $\bar{x} = [\bar{r}, \bar{v}] = [x, y, z, \dot{x}, \dot{y}, \dot{z}]$. Throughout the document, overbars denote vector quantities. The characteristic length (l^*) is defined as the distance between the primaries, the characteristic mass (m^*) is the sum of the primary masses, and the characteristic time (t^*) is defined such that the mean motion of the primaries $\dot{\theta}$ is equal to 1. The nondimensional mass ratio, defined $\mu = m_2/m^*$, is a governing characteristic of the system dynamics. With this formulation, the equations of motion are written in nondimensional rotating coordinates as

$$\ddot{x} = 2\dot{y} + \frac{\partial U^*}{\partial x}, \qquad \ddot{y} = -2\dot{x} + \frac{\partial U^*}{\partial y}, \qquad \ddot{z} = \frac{\partial U^*}{\partial z}. \tag{1}$$

In Eq. (1), U^* is the pseudopotential function, defined

$$U^* = \frac{1-\mu}{r_{13}} + \frac{\mu}{r_{23}} + \frac{1}{2}(x^2 + y^2), \tag{2}$$

where $\bar{r}_{ij} = \bar{r}_j - \bar{r}_i$ and an omitted overbar represents the scalar magnitude of the vector, i.e., $r_{ij} = |\bar{r}_{ij}|$. Five equilibrium points, the Lagrange points or libration points, exist in the CR3BP model, denoted L_i for $i = 1, ..., 5$. The CR3BP equations of motion admit one integral, an energy-like quantity denoted the Jacobi Constant. This integral is defined as $C = 2U^* - v^2$, where v is the nondimensional velocity magnitude as it appears in the rotating frame.

Higher-Fidelity Ephemeris Model

The HFEM is a representation of the N-body problem in which positions of the celestial bodies are extracted from a database of ephemerides. Employing ephemeris data increases the fidelity of the model to better represent the forces a spacecraft might experience for a given mission and time frame. The relative equations of motion are formulated in an inertial frame referenced to a central body, expressed

$$\ddot{\bar{r}}_{cs} = -G\frac{(m_c + m_s)}{r_{cs}^3}\bar{r}_{cs} - G\sum_{i=1}^{n} m_i \left(\frac{\bar{r}_{ci}}{r_{ci}^3} - \frac{\bar{r}_{si}}{r_{si}^3}\right), \tag{3}$$

where $\ddot{\bar{r}}_{cs}$ denotes the acceleration of the spacecraft S relative to the central body C resulting from the gravitational pull of the central body and the remaining n bodies. The celestial bodies are assumed point masses and no forces beyond gravity from the included set of bodies are modeled. Positions of the bodies are obtained from the DE440 planetary ephemerides within the NASA JPL Navigation and Ancillary Information Facility database.[10] In this investigation, states are propagated in a Moon-centered J2000 reference frame, incorporating the gravitational influences of the Sun, Earth, and Moon.

BACKGROUND

The current investigation further develops concepts previously introduced by Nugent and Howell.[11] Along a trajectory of an arbitrary time horizon, the state transition matrix (STM) is produced by evolving the linear variational equations and including the variational partials during numerical integration. The STM is a first-order approximation of the variational flow near the reference, offering a convenient foundation for describing nearby relative motion. In the authors' original investigation, the STM is divided into four 3x3 sub-matrices that represent the different combinations available to isolate sub-phases of state variations for a reference arc propagated from time t_0 to time t, i.e.,

$$\boldsymbol{\Phi}(t, t_0) = \begin{bmatrix} \boldsymbol{\phi}_{r,r} & \boldsymbol{\phi}_{r,v} \\ \boldsymbol{\phi}_{v,r} & \boldsymbol{\phi}_{v,v} \end{bmatrix}. \tag{4}$$

In Eq. (4), the first subscript for each 3x3 sub-matrix denotes the state isolated at the final time – either position (r) or velocity (v) – and the second subscript indicates the initial variation. For example, the $\boldsymbol{\phi}_{r,v}$ sub-matrix isolates the effect of a maneuver at the initial time, t_0, on the resulting relative position variation at the final time, t; equivalently, $\boldsymbol{\phi}_{r,v} = \partial \bar{r} / \partial \bar{v}_0$. Principal stretching and restoring direction information is produced through the singular value decomposition (SVD) of one of the STM sub-matrices, depending on the application of interest. The singular value decomposition characterizes a linear mapping represented by a matrix as a series of rotations and scaling, and, in the process, identifying the directions of most and least stretching. In this application, the SVD yields the principal stretching directions for the phase space near the baseline path. The stretching directions associated with the initial time, $\bar{V}_i$, are the right singular vectors of the STM and map to the stretching directions corresponding to the final time or left singular vectors, $\bar{U}_i$, subject to a scaling factor given by the singular values σ_i. For any of the four sub-matrices in Eq. (4), the 3-dimensional stretching directions form orthonormal vector bases that span the phase space at both the initial and final times. This choice of vector basis admits relative state characterizations that are informed by the natural dynamics. For an arbitrary 3x3 sub-STM, the authors derive an equation to relate the magnitudes of state variations at the endpoints of the baseline arc,[11] i.e.,

$$\alpha_1^2(\gamma^2 - \sigma_1^2) + \alpha_2^2(\gamma^2 - \sigma_2^2) + \alpha_3^2(\gamma^2 - \sigma_3^2) = 0, \tag{5}$$

where σ_i are the singular values for the current subset the STM, α_i are the measure numbers for the initial state variation expressed in the $\bar{V}_i$ frame, and γ is the variation magnitude ratio. For the previous spacecraft loitering application that leverages the $\boldsymbol{\phi}_{r,r}$ matrix, this ratio is defined $\gamma = \delta r_f / \delta r_0$, relating the variational distance of a deputy spacecraft from the chief spacecraft at the two endpoints. Thus, solutions to Eq. (5) provide deputy spacecraft starting locations for which the ballistic trajectory evolution is predicted to result in a final distance equal to $\delta r_f = \gamma \delta r_0$. From this formulation, a methodology is derived to identify feasible deputy spacecraft starting locations yielding ballistic relative trajectories that remain between prescribed minimum and maximum separation distances throughout a loitering phase. The analysis relies relies on the linear representation of the variational phase space. In their preliminary investigation, Nugent and Howell also include a brief introduction to demonstrate a similar formulation to plan impulsive maneuvers for collision avoidance. The specifics of this collision avoidance strategy are further developed here, in addition to a more thorough evaluation of the methodology across sample multi-body orbits.

COLLISION AVOIDANCE FORMULATION

The previous derivation for $\boldsymbol{\phi}_{r,r}$ leverages useful properties of a 3x3 STM, but there is no requirement that the related states are components only of position. Velocity and position are interchangeable without any necessary modifications to the governing relationship in Eq. (5). Collision avoidance serves as another useful application for this approach, as the current perspective offers insight into the natural evolution of relative behaviors. Consider a scenario in which a spacecraft operates in a multi-body orbit and a collision is predicted with another space object at some future time. The conjunction event must be prevented, however, it is desired that the spacecraft naturally returns close to the reference path after the collision is successfully avoided. At any given moment, it is only possible to directly adjust the velocity of the spacecraft. While many

initial maneuver directions are available that eliminate the conjunction risk, only a subset naturally return the spacecraft to a position near the reference path and at the proper phase. This application lends itself to the 3×3 $\boldsymbol{\phi}_{r,v}$ sub-matrix of the STM, evaluating the effect of an impulsive change in the initial velocity on the downstream position variation.

Employing the $\boldsymbol{\phi}_{r,v}$ matrix for the current application implies that Eq. (5) relates initial maneuver directions to final position directions. The interpretation of this SVD information changes for collision avoidance. The ratio γ and the singular values σ_i are intuitive as nondimensional distance ratios in the loitering application, but are no longer intuitive in nondimensional units for this mixed-phase case. As a result, it is insightful to dimensionalize the STM. Recall that $\boldsymbol{\phi}_{r,v}$ relates an initial velocity variation to a final position variation as

$$\delta\bar{r}_f = \boldsymbol{\phi}_{r,v}(t_f, t_0)\delta\bar{v}_0. \tag{6}$$

In Eq. (6), the vectors $\delta\bar{r}_f$ and $\delta\bar{v}_0$ are nondimensionalized by the CR3BP characteristic values of length and time, l^* and t^*. Assuming distance is measured in kilometers and velocity in meters per second, the relationships between dimensional and nondimensional quantities are expressed $[\delta\bar{r}_f]_{ndim} = [\delta\bar{r}_f]_{km} * (1/l^*)$ and $[\delta\bar{v}_0]_{ndim} = [\delta\bar{v}_0]_{m/s} * (1e3 * t^*/l^*)$. Substituting these expressions into Eq. (6) yields an analogous relationship between dimensional quantities,

$$[\delta\bar{r}_f]_{km} = [\boldsymbol{\phi}_{r,v}]_{ndim}\left(\frac{t^*}{1e3}\right)[\bar{v}_0]_{m/s}. \tag{7}$$

The scaling factor in Eq. (7) permits a relationship between an initial maneuver in m/s to a later distance variation in km. Thus, the dimensional STM is defined

$$[\boldsymbol{\phi}_{r,v}]_{km/(m/s)} = [\boldsymbol{\phi}_{r,v}]_{ndim}\left(\frac{t^*}{1e3}\right). \tag{8}$$

The elements of the dimensional STM in Eq. (8) and their resulting singular values possess units of km/(m/s). Furthermore, these dimensional singular values are scaled by the initial maneuver magnitude, producing values in units of km. For the current collision avoidance application, these scaled, dimensional singular values are defined

$$\varsigma_i = \Delta v[\sigma_i]_{km/(m/s)}, \tag{9}$$

where $[\sigma_i]_{km/(m/s)}$ are the singular values of the matrix $[\boldsymbol{\phi}(t_f, t_0)_{r,v}]_{km/(m/s)}$, Δv is measured in m/s, and ς_i is expressed in km. With singular values in units of distance, it is now straightforward to directly relate the SVD information with any constraints imposed on the isochronous distances along the diverted trajectory. Adapting Eq. (5) for values in km results in the relationship

$$v_1^2(r_{constraint}^2 - \varsigma_1^2) + v_2^2(r_{constraint}^2 - \varsigma_2^2) + v_3^2(r_{constraint}^2 - \varsigma_3^2) = 0, \tag{10}$$

where $r_{constraint}$ represents a distance constraint on the diverted trajectory in km (e.g., a safe miss distance) and ς_i are the scaled, dimensional singular values. The terms v_i represent measure numbers analogous to α_i, but are now in units of m/s and correspond to $\bar{V}_i$ basis vectors for the initial maneuver. Note that Eq. (10) supplies identical information to Eq. (5), but in dimensional quantities that are more easily interpreted for this mixed-phase application.

Consistent with the authors' original investigation into spacecraft loitering, solutions to Eq. (10) emerge in the form of elliptic cones. The design parameter for the current application is the variable $r_{constraint}$, bounded below by ς_3 and above by ς_1. When this parameter is selected outside of these bounds, the solution to Eq. (10) is no longer real-valued. From the definition of the SVD, ς_3 and ς_1 are known to bound the available natural behavior. Figure 1 depicts sample solutions for discrete values of $r_{constraint}$ for a 50-hour segment along the 9:2 NRHO beginning at apolune. In this example, the scaled, dimensional singular values of $\boldsymbol{\phi}_{r,v}(t_f, t_0)$ are equal to $\varsigma_1 = 215$ km, $\varsigma_2 = 171$ km, and $\varsigma_3 = 157$ km for an initial maneuver of magnitude 1 m/s. The elliptic cones in velocity space denote the full set of solutions for a 1 m/s maneuver at apolune that result in the selected distance at the final time of 50 hours post-maneuver, indicated by the legend. These

cones are centered around either $\bar{V}_3$ (for $r_{constraint} < \varsigma_2$) or $\bar{V}_1$ (for $r_{constraint} > \varsigma_2$). Mapping the surfaces to position space at the final time yields the distances predicted by the linear mapping. A sample maneuver from each surface is applied as a velocity change to the reference state and propagated using the nonlinear CR3BP equations of motion. The resulting isochronous distances from the reference are plotted in Figure 2, demonstrating that the nonlinear results match the linear predictions. Maneuvers are also simulated in the $\bar{V}_1$ and $\bar{V}_3$ directions and plotted in red and blue, respectively, bounding the remaining trajectories at the final time. Final distances may also be constrained between lower and upper bounds through inequality constraints within Eq. (10), in the same manner that motion is bounded in the spacecraft loitering case. Any maneuver that exists between two surfaces corresponding to $r_{constraint,1}$ and $r_{constraint,2}$ is predicted to arrive between these two bounds, i.e., $r_{constraint,1} < r_f < r_{constraint,2}$.

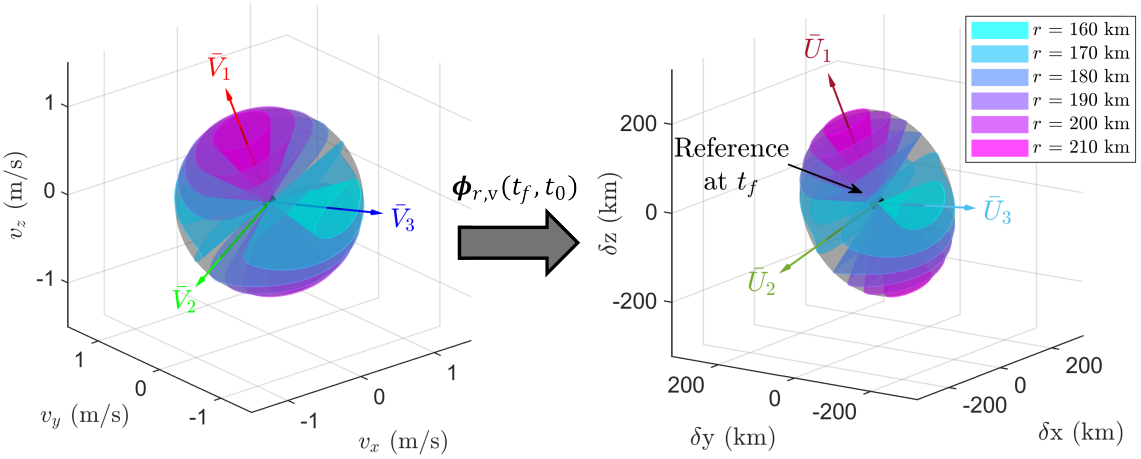

Figure 1: Mapping of $\boldsymbol{\phi}_{r,v}$ quadric solution surfaces for a 50-hour segment along the 9:2 NRHO beginning at apolune. Surfaces at the initial time are in velocity space and final-time surfaces are in position space.

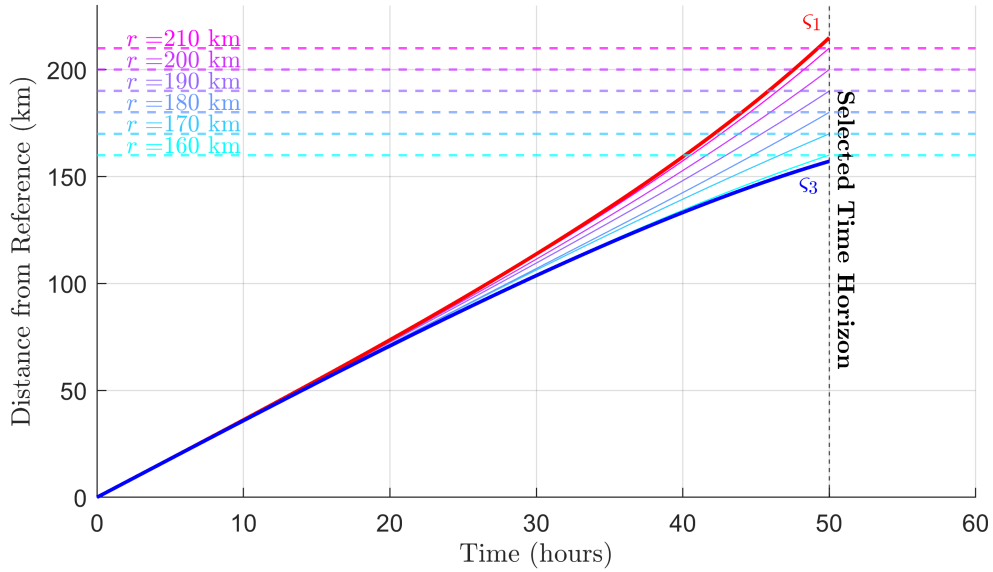

Figure 2: Validation for predicted behavior via CR3BP nonlinear propagation.

MANEUVER PLANNING METHODOLOGY

Favorable diverted trajectories are determined by evaluating two conditions, as depicted in Figure 3. The first condition dictates that a minimum separation distance, r_{miss}, is achieved between the diverted spacecraft trajectory and the point at which the hazardous object is predicted to intersect the reference orbit. This condition is evaluated at the conjunction or 'miss' time horizon, t_{miss}. Condition 2 enforces the requirement that the spacecraft later returns toward the reference path in position space to within a maximum distance, r_{return}. Distance variations from the reference trajectory are measured with an isochronous correspondence and the 'return' time horizon for this condition, t_{return}, denotes the time elapsed in both the diverted trajectory and the baseline arc. Therefore, as t_{return} is adjusted, the reference point from which this maximum distance must be achieved also shifts along the baseline. The two conditions are assessed as inequalities, isolating interior or exterior regions of elliptic cones dictated by Eq. (10) at the two specified time horizons. It is worth noting that the remaining path of the hazardous space object is not currently incorporated into the avoidance methodology. However, appropriate selection of the miss distance and the inherent flexibility of resulting maneuver options allows for some control to account for this complication.

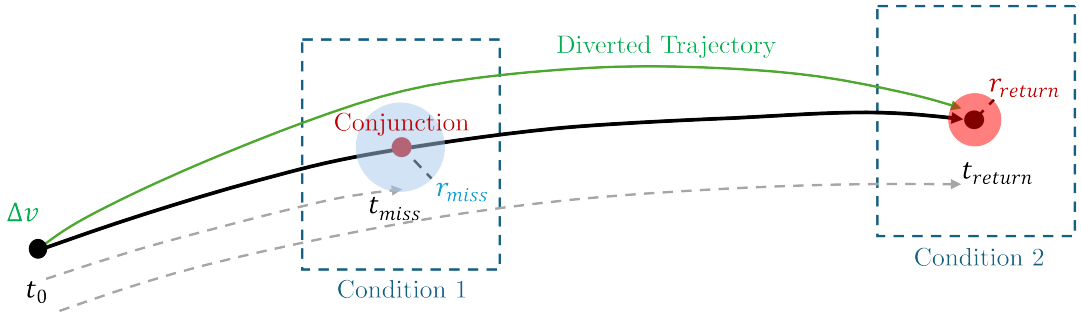

Figure 3: Illustration of conditions imposed on diverted trajectories for collision avoidance.

A strategy is developed to determine the initial maneuvers that meet the two specified conditions to yield a feasible trajectory diversion. In practice, the time to predicted collision is based on the situation and cannot be selected arbitrarily. Assuming this miss time horizon, t_{miss}, is known, the process to determine favorable maneuver directions consists of the following steps:

1. Select an acceptable minimum separation distance from the space object (r_{miss}) and a maximum isochronous distance for return to the reference path (r_{return}).
2. Estimate the required initial maneuver magnitude assuming a linear relationship ($\Delta v = r_{miss}/t_{miss}$).
3. Select a maximum return time horizon by which the spacecraft should be near the reference orbit ($t_{return,max}$). This value denotes the time elapsed in both the reference and diverted arcs.
4. Propagate the reference state and STM from t_0 to $t_{return,max}$ and evaluate the singular values corresponding to the dimensional $\boldsymbol{\phi}_{r,v}(t_j, t_0)$ sub-matrix for intermediate times t_j.
5. Scale the $\boldsymbol{\phi}_{r,v}$ singular values by the maneuver magnitude Δv and identify time horizons when the smallest scaled singular value (ς_3) is below the value r_{return}; these time horizons serve as candidates for the return time, t_{return}.
6. Iterate through the candidate return times chronologically, evaluating the bounding surfaces from the stretching directions at the initial time, $\bar{V}_i$, corresponding to the two conditions (r_{miss} and r_{return}).
7. Select the first candidate return time horizon that yields a local maximum of overlapping burn directions for the two conditions.

Maneuver directions that meet both inequality conditions in step 6 are predicted to sufficiently avoid the space object and return to within close proximity of the reference path in an appropriate time interval. In step 7, the first t_{return} corresponding to a local maximum is selected to reduce the extent of the diversion from the baseline orbit and routine operations while still offering flexibility in the maneuver directions. If time spent along a diverted arc is less important than maneuver flexibility, the remaining candidates for t_{return} offer opportunities for comparison. In this preliminary investigation, it is assumed that errors in the return state are corrected by standard orbit maintenance procedures.

As an example, consider a spacecraft operating in an Earth-Moon butterfly orbit. Suppose a space object is predicted to collide with the spacecraft 36 hours downstream from its current location, and a minimum safe distance of 100 km is required. An initial impulsive maneuver of magnitude 0.772 m/s is examined in all possible directions. For operational reasons, it is decided the spacecraft must return to routine operations within at most the next two revolutions of the orbit ($t_{return,max} = 2$ revs). The scaled, dimensional ς_3 is produced after numerical propagation of the STM from the maneuver time to $t_{return,max}$ and appears in Figure 4. In the figure, at each time the value of ς_3 dips below 50 km, the curve is colored in blue. Recall from the definition of the SVD and stretching directions that the smallest singular value provides the linear prediction for the minimum achievable variation at the evaluated time horizon. Thus, it is not necessary to check time horizons for which ς_3 is above the return value of 50 km, as solutions are not possible. Times corresponding to the blue points are evaluated as candidate return times (t_{return}). Return times at which solutions exist – meaning the burn directions identified for the miss and return conditions overlap – are further denoted in green. During the first time segment where solutions exist (between 0.3 and 0.4 revolutions downstream), t_{return} is selected at the time when the overlapping region reaches a local maximum; in this case t_{return} = 0.35 revolutions, or about 8 days, after the maneuver. The baseline orbit in this example is the same as the butterfly reference orbit described later, with the maneuver occurring 3.9 days before the farside apolune.

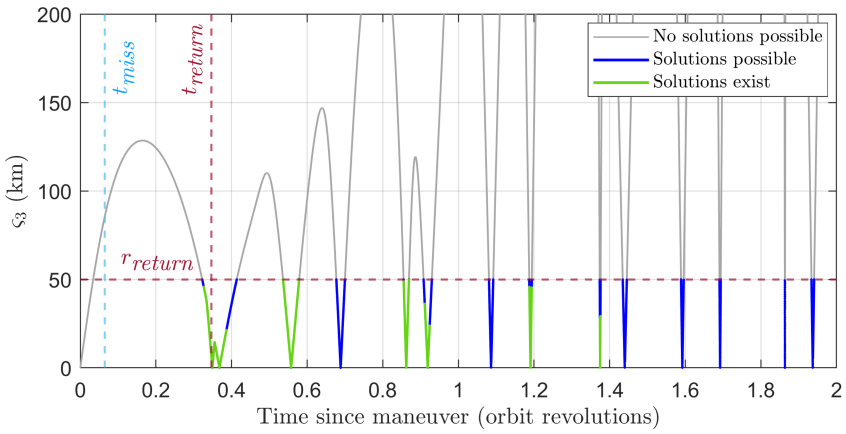

Figure 4: Evaluation of candidate return time horizons along a butterfly orbit.

The sphere representing all possible initial maneuver directions of magnitude 0.772 m/s appears in Figure 5(a). The bounding surfaces corresponding to r_{miss} and r_{return} for the two specified time horizons appear in the figure. For r_{miss}, the inequality constraint dictates that any direction interior to the blue conical surface is predicted to meet Condition 1. For r_{return}, only directions exterior to the red cone are predicted to meet Condition 2. The overlap of these regions, colored green, denotes the linear prediction for the full solution space for directions representing a 0.772 m/s burn that meet the two determined conditions. Sample feasible maneuver directions determined in Figure 5(a) are applied as a velocity change to the initial reference state and then propagated using the CR3BP nonlinear dynamics. The isochronous distance between each diverted trajectory and the reference orbit is evaluated from the nonlinear propagation and is plotted over time in Figure 5(b). The miss and return distances and times are included in the figure as dashed lines for reference. The nonlinear results demonstrate that the diverted arcs successfully avoid the conjunction event and then

naturally return close to the reference orbit. Note that a small subset of the arcs in Figure 5(b) conclude with isochronous distances slightly above the selected upper bound. Inaccuracies between the linear prediction and the nonlinear propagation are anticipated and are inspected in more detail later. Any errors in nonlinear behavior may be corrected through a targeting scheme once the linear results are available.

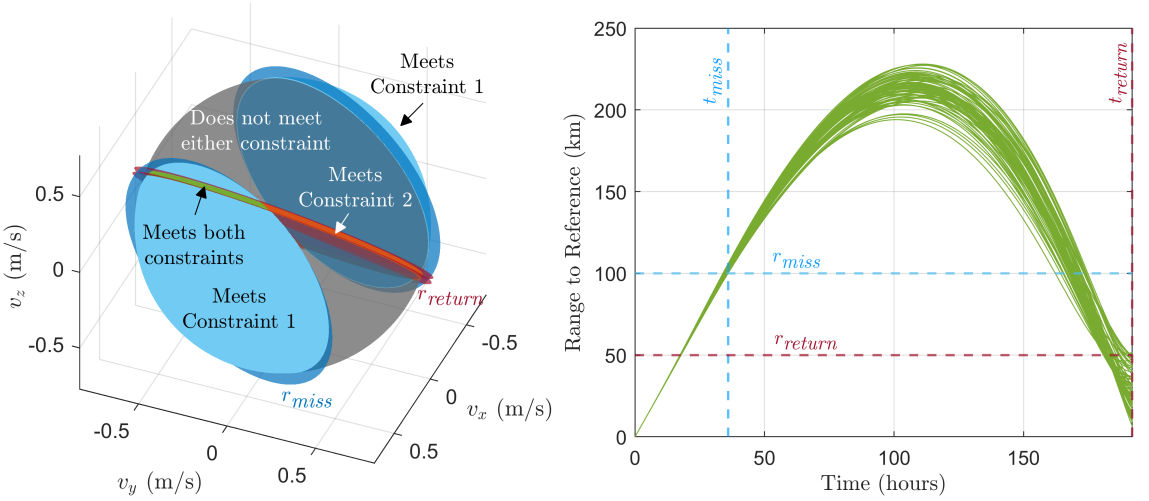

(a) Evaluation of feasible maneuver directions.

(b) Validation for diverted trajectories via CR3BP nonlinear propagation.

Figure 5: Example determination of feasible collision avoidance maneuvers along a butterfly orbit.

SIMULATION PARAMETERS

Collision avoidance scenarios are simulated numerically in the Earth-Moon CR3BP to assess the proposed relative trajectory design methods. Reference trajectories are selected as segments of periodic orbits to mimic realistic mission scenarios. A spacecraft is assumed to move along the reference periodic orbit until a collision is predicted downstream with an encroaching space object, upon which an impulsive maneuver is implemented to avoid the collision and then return toward the reference. The linear analysis is accomplished via the STM evaluated along the reference path as previously described, and resulting behaviors are validated through propagation of the nonlinear CR3BP EOMs.

Reference Orbits

Two periodic orbits in the Earth-Moon CR3BP are employed as reference trajectories for modeling collision avoidance scenarios. The first orbit selected for investigation is the southern 9:2 synodic resonant NRHO. As previously mentioned, the 9:2 NRHO is the intended baseline trajectory for the NASA Gateway space station as part of the Artemis program. It is a nearly-stable member of the L_2 halo family with a close passage above the lunar north pole and uninterrupted line of sight with Earth. The orbital perilune and apolune are roughly 3,500 and 71,000 km from the center of the Moon, respectively, with a period near 6.5 days. The second selected orbit is an unstable member of the P2HO1 ("butterfly") orbit family.[12] The butterfly orbit possesses four local apolunes and perilunes, with a maximum apolune distance of 64,000 km and minimum perilune distance of 44,000 km, both on the lunar farside. The period of the orbit is approximately 23 days. The two reference orbits are plotted in Figure 6 with arrows indicating the directions of motion. A trigonometric encoding angle is selected to represent the starting location of the spacecraft on the periodic reference orbit, defined

$$\xi = \frac{t_{po} * 360^o}{\mathbb{P}}, \tag{11}$$

where t_{po} is the time elapsed since a reference location on the orbit and $\mathbb{P}$ is the period of the orbit. The encoding angle ranges from 0 to 360 degrees and is analogous to mean anomaly, but applicable to non-

Keplerian orbits such as many orbits of interest in the CR3BP. Reference locations along the two orbits are included in Figure 6, denoted by an angle of zero; both correspond to apolunes.

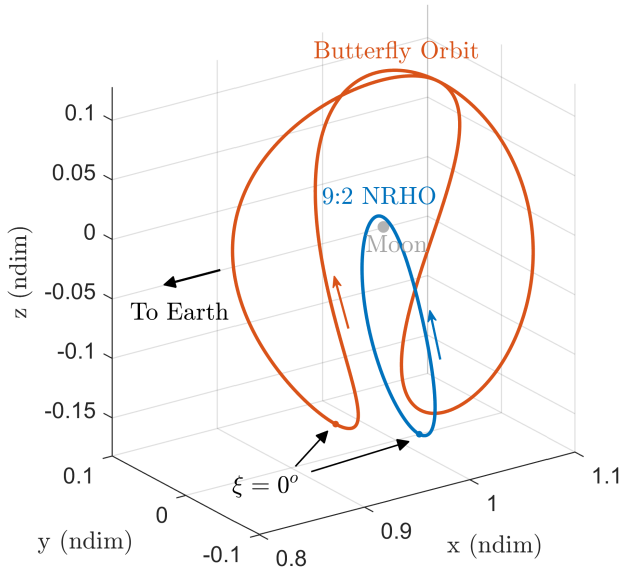

Figure 6: Reference periodic orbits in the Earth-Moon CR3BP.

Test Cases and Performance Metrics

Two test cases are defined to assess the effectiveness of the maneuver planning methodology along the selected reference orbits. In a true flight scenario, various parameters are determined directly by the circumstances and operational constraints. For example, the time until predicted collision is contingent upon when the object is detected. The minimum acceptable separation distance is likely dependent on the tracking solution for the encroaching space object and informed by a statistical analysis of the collision probability.[13] As a simplification for this investigation, representative values are accessed from the literature. Davis et al. analyze collision avoidance scenarios with miss distances ranging from 25 to 200 km and miss time horizons ranging from 12 to 48 hours.[8] An intermediate miss distance (r_{miss}) of 100 km is employed for all current test cases while varying the miss time (t_{miss}). A constant value is selected here to prioritize minimizing collision risk over fuel savings. The maximum return distance is selected as 50 km for all cases, well within the range of typical isochronous position errors in successful libration point orbit stationkeeping strategies.[14] Recall that the return time (t_{return}) is determined case-by-case as detailed in the methodology steps, limited here to at most three revolutions downstream along the reference orbit. The collision avoidance simulation parameters are summarized in Table 1.

Table 1: Maneuver planning methodology test cases.

	Case 1	Case 2
Time to predicted collision (t_{miss})	24 hours	36 hours
Minimum miss distance (r_{miss})	100 km	100 km
Resulting maneuver magnitude (Δv)	1.157 m/s	0.772 m/s
Maximum return distance (r_{return})	50 km	50 km
Maximum return time ($t_{return,max}$)	3 revs	3 revs

The performance for collision avoidance maneuver (CAM) availability is evaluated through a few primary metrics. The most basic metric is a binary value to indicate whether the linear analysis yields any maneuver directions that meet both the miss and return constraints. A successful test implies that at least one maneuver direction exists at the initial time such that the resulting diverted trajectory is predicted to adequately miss

the space object at t_{miss} and naturally return sufficiently close to the reference path at a later time. An unsuccessful test implies that a single-maneuver collision avoidance strategy is likely not feasible for the given set of conditions. The second performance metric is the percentage of the spherical surface area spanned by the feasible burn directions at the determined maneuver magnitude. This metric is indicative of the flexibility of initial burn directions, which could increase the diversity of available relative trajectory geometries or serve as a safety measure in case of burn implementation error. For cases where feasible burn directions are identified, a subset of these initial conditions are propagated under the CR3BP nonlinear EOMs. The percentage of nonlinear trajectories that meet both of the imposed constraints serves to evaluate the accuracy of the linear prediction. The time horizon determined for the return condition (i.e., t_{return}) is also evaluated as a performance metric, with a preference for reducing the extent of the trajectory diversion. Lastly, the relative velocity magnitudes upon return near the reference are assessed. In a mission scenario, off-nominal velocities after the diversion are potentially corrected through routine stationkeeping operations or via a dedicated post-arrival maneuver. Inspecting the final-time velocities provides insight into potential fuel costs resulting from the diversion beyond the initial avoidance burn.

CR3BP RESULTS

24-hour Miss Time Horizon

Results for a 24-hour time horizon until predicted collision appear in Figures 7 and 8 for the two reference orbits. Recall that the 'percentage of feasible maneuver directions' refers to the proportion of initial directions in 3D velocity space for which a single impulsive maneuver of magnitude 1.157 m/s is predicted to provide the necessary minimum separation from the hazardous space object and naturally return to the reference orbit within the prescribed maximum distance and with the proper phase. These percentages along the 9:2 NRHO appear in Figure 7, plotted against the starting location along the orbit, i.e., the location where the maneuver is performed. The same data is also overlaid onto the orbit to better visualize the starting locations. The maximum percentage of feasible burn directions reaches 0.59%, corresponding to the region surrounding apolune ($\xi = 0$). A gap in the available solutions exists at perilune, beginning immediately prior to the closest lunar approach and extending asymmetrically about the line of apsides to an encoding angle of 245 degrees. Results for the butterfly orbit appear in Figure 8. The maximum percentage for maneuver flexibility along this orbit 0.54%. There are two gaps in the solution curves that occur between 13 to 33 degrees and 194 to 223 degrees initial encoding angle. The solution gaps are not clearly associated with close lunar approaches. There is one distinct peak in availability near 120 degrees, with no clearly mirrored behavior within the other lobe of the orbit.

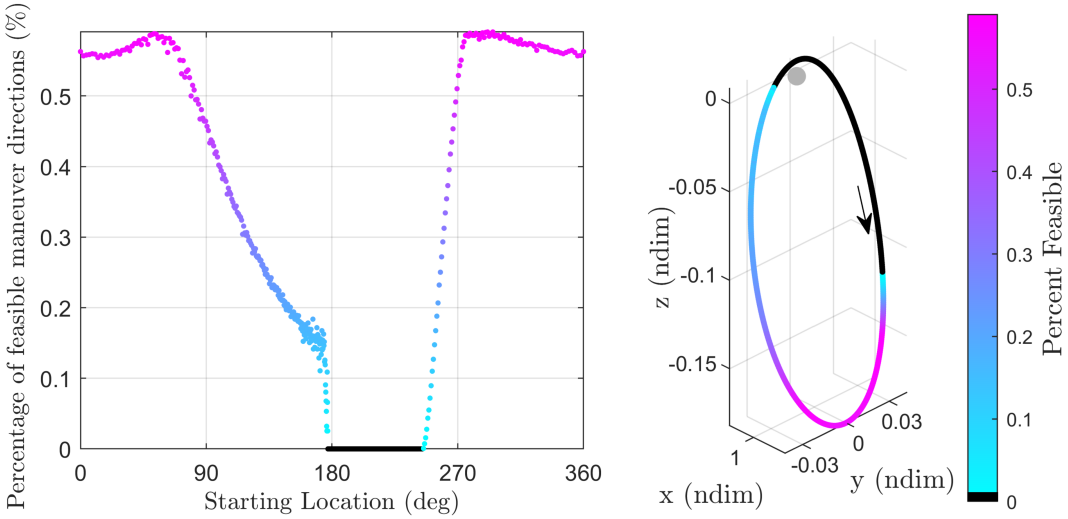

Figure 7: Evaluation of feasible maneuver directions along the NRHO for a 24-hour miss time.

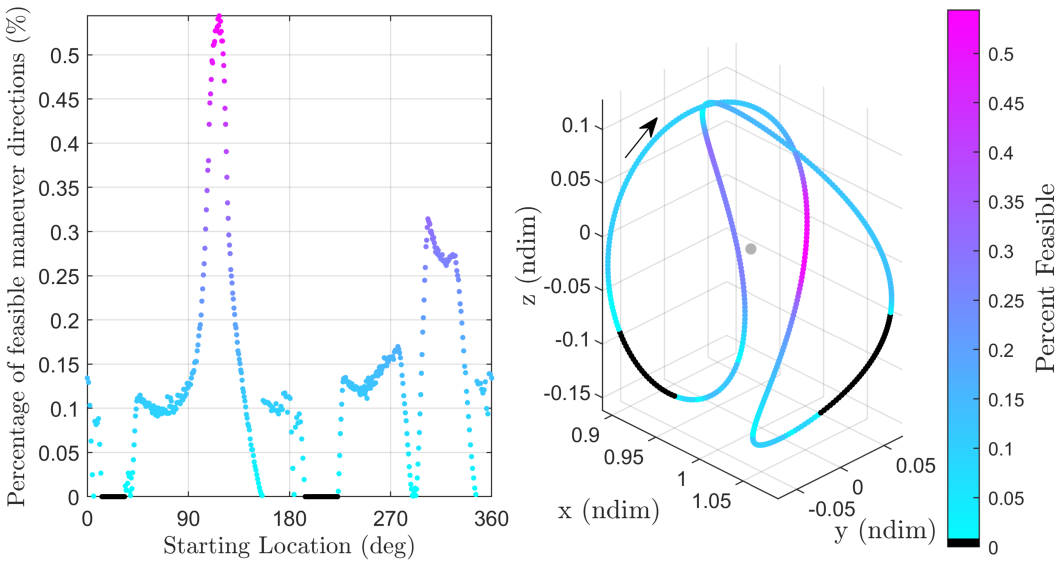

Figure 8: Evaluation of feasible maneuver directions along the butterfly orbit for a 24-hour miss time.

The return times resulting from the maneuver planning methodology appear in Figure 9. In Figure 9(a), the data is presented in dimensional units of days post-maneuver and Figure 9(b) renders the same data in terms of revolutions of the underlying orbit. Recall that the return time is selected at the first local maximum in overlapping maneuver directions for the miss and return conditions. A sudden increase in return time indicates a disappearance of any solutions at the previous time. Conversely, a sudden drop denotes the emergence of an earlier solution. Values for the return time along the NRHO oscillate near one revolution of the orbit. Near perilune in the NRHO, the return times jump to nearly 12 days. For the butterfly orbit, times are generally under 12 days. One notable exception occurs near 30 degrees, where return times extend as high as 19 days. As a function of orbital period, all return times for the butterfly orbit are under one revolution.

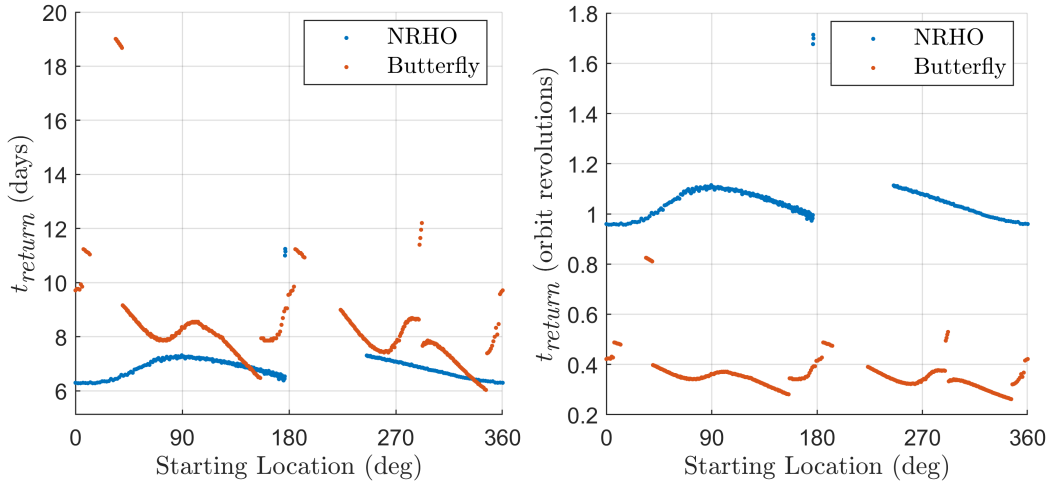

(a) Return times in days.

(b) Return times in orbit revolutions.

Figure 9: Return times identified during evaluation for a 24-hour miss time.

For every starting location along the two reference orbits, each available maneuver option is mapped to the final time via the $\boldsymbol{\phi}_{v,v}(t_{return}, t_0)$ matrix to determine the range of relative return velocities resulting from the diverted trajectories. These variational return velocity magnitudes are plotted in Figure 10 for each orbit, denoting the minimum, maximum, and average associated values. Recall that the collision avoidance maneuver at this miss time is 1.157 m/s. For the NRHO, the final variational velocity magnitudes range between 0.5 and 2.5 m/s, yielding a broader dispersion near perilune. Values along the butterfly orbit range from 0

to 4 m/s with a notable jump above 6.5 m/s in the same region of the orbit where the return times increase dramatically. Inspection of the relative return velocities highlights the fact that, while the collision avoidance methodology considers only a single maneuver at the initial time, the effect of the trajectory diversion on fuel expenditure extends beyond the initial maneuver and more investigation is warranted.

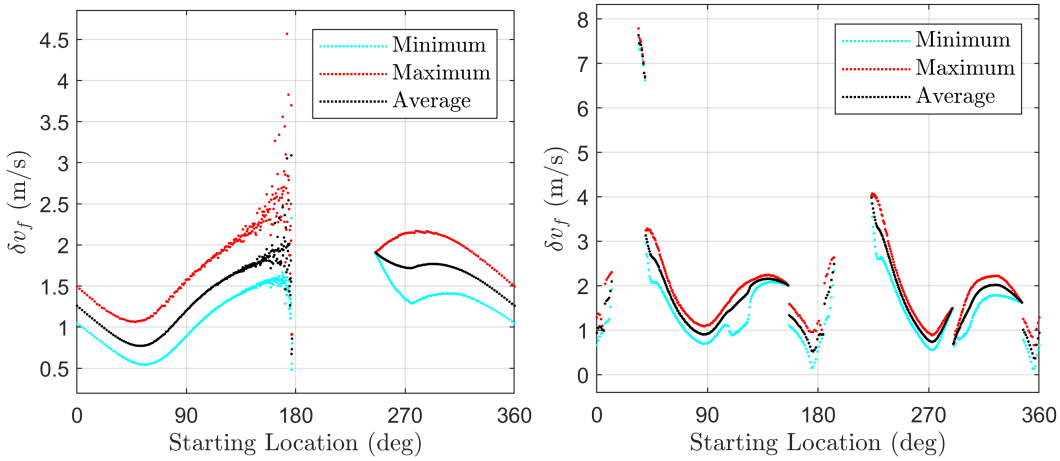

(a) Relative return velocities along NRHO. (b) Relative return velocities along butterfly orbit.

Figure 10: Relative velocity magnitudes at return condition for a 24-hour miss time.

36-hour Miss Time Horizon

The miss time horizon, i.e., the time from the maneuver until the predicted collision, is adjusted to 36 hours and the collision avoidance methodology is reevaluated for the two reference orbits. A result of increasing the miss time is a reduction in the required maneuver magnitude, hence, the tests now examine a maneuver of magnitude 0.772 m/s. The percentages of available CAM directions appear in Figures 11 and 12. Across both orbits, the primary benefit of increasing the miss time is an increased flexibility of the feasible solutions, with similar overall behaviors as emerged when the miss time was 24 hours. The highest percentage of available maneuver directions along the NRHO now extends above 1.3%, double the previous test case. The maximum percentage along the butterfly orbit also increased, but by a lesser amount, just under 0.7%. In addition, a second local maximum emerges in Figure 12 at an orbital starting location near 300 degrees, of similar magnitude to the first. For both orbits, the gaps in the solutions persist but are shifted slightly left

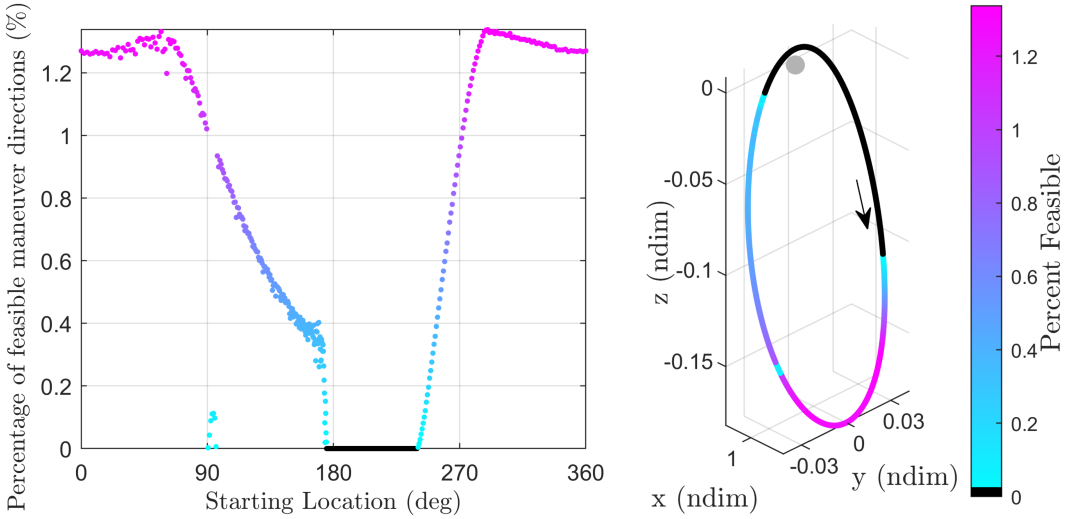

Figure 11: Evaluation of feasible maneuver directions along the NRHO for a 36-hour miss time.

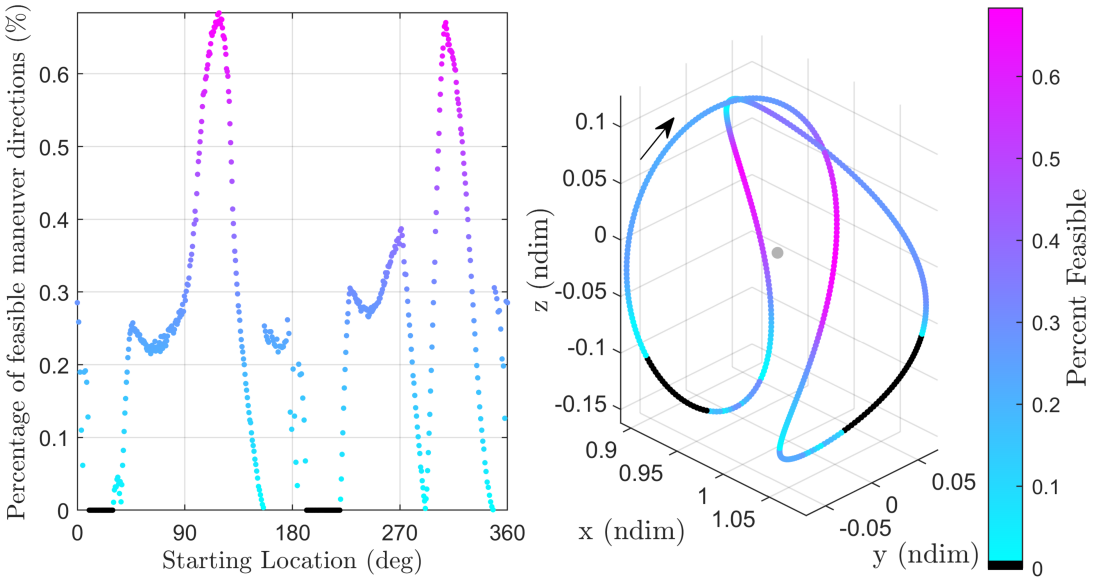

Figure 12: Evaluation of feasible maneuver directions along the butterfly orbit for a 36-hour miss time.

with the increase in the miss time horizon. Information regarding the return time horizons identified in the process appears in Figure 13. The return times are almost identical to those from Figure 9. Jumps in return times are still present for both orbits, near 30 degrees in the butterfly orbit and immediately prior to perilune in the NRHO.

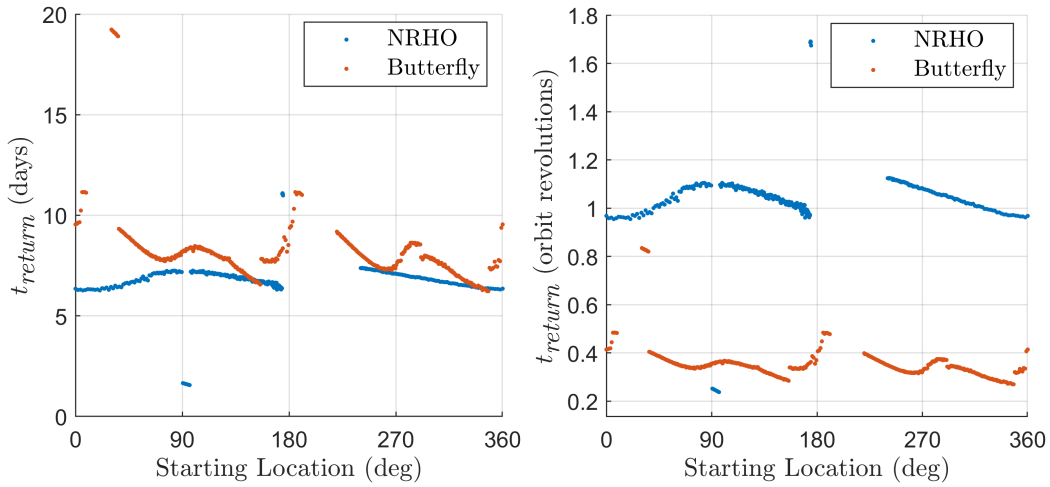

(a) Return times in days.

(b) Return times in orbit revolutions.

Figure 13: Return times identified during evaluation for a 36-hour miss time.

Variational velocity magnitudes at the return condition for the 36-hour miss time horizon are plotted in Figure 14. The reduction in the initial maneuver magnitude generally also reduces the relative return velocities. Along the NRHO, most of the return velocity variations are under 2 m/s. However, a new jump appears in the NRHO data near 100 degrees where velocities reach 10 m/s, corresponding to the region in the orbit where the return times also drop with the emergence of earlier solutions. This result indicates that, while there may be solutions that return toward the reference more quickly, it is potentially more cost-effective to explore later arrival times. The butterfly orbit relative return velocities follow patterns that are similar to the 24-hour case, with magnitudes now generally under 3 m/s, and the outlier region around 5 m/s.

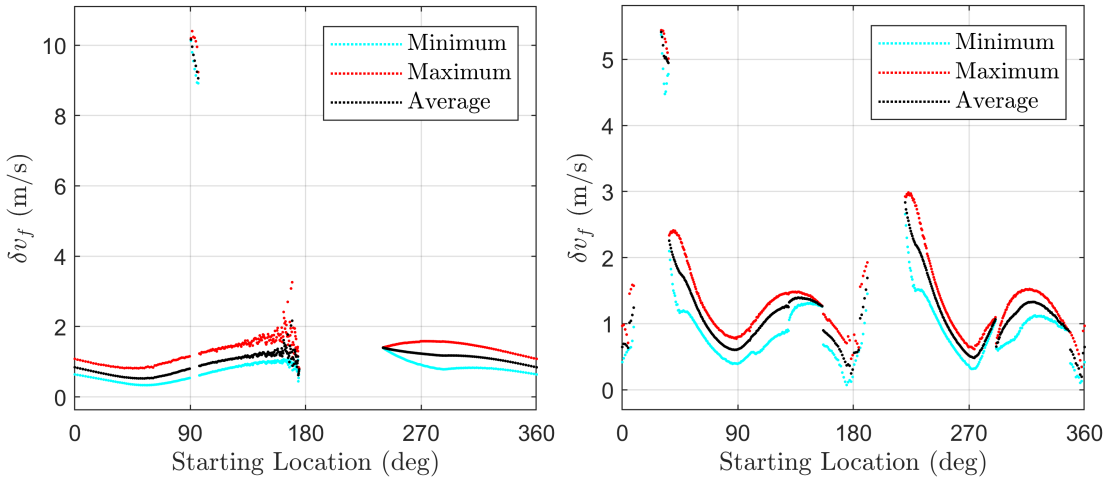

(a) Relative return velocities along NRHO. (b) Relative return velocities along butterfly orbit.

Figure 14: Relative velocity magnitudes at return condition for a 36-hour miss time.

To visualize the solutions, sample feasible maneuver directions at the 36-hour miss time horizon are depicted in Figures 15 and 16. Inspecting Figure 15(c) offers insight into the nature of determining solutions for the two conditions. In general, the miss condition is met by a large proportion of the candidate maneuver directions due to the short time horizon and the strategy employed to select the maneuver magnitude. As a result, the return condition is the more limiting constraint. As possible return times are assessed, solutions appear when the interior of the conical surface corresponding to the return condition overlaps with the fixed miss condition region, governed primarily by the direction of the $\bar{V}_3$ singular vector. In Figure 15(c), a maximum in the number of feasible directions occurs when the return region still overlaps the miss condition surface, evident from the missing portion of the elliptical region. Between this starting location and the previous segment of the orbit where solutions do not exist, this region continues to shift toward the directions that are predicted not to meet the miss constraint. Figure 16(c) illustrates another sample scenario where the return region is reduced by the miss condition. In this case, the return condition forms a ring around the entire sphere of candidate directions, but is cut off by the surface corresponding to r_{miss}.

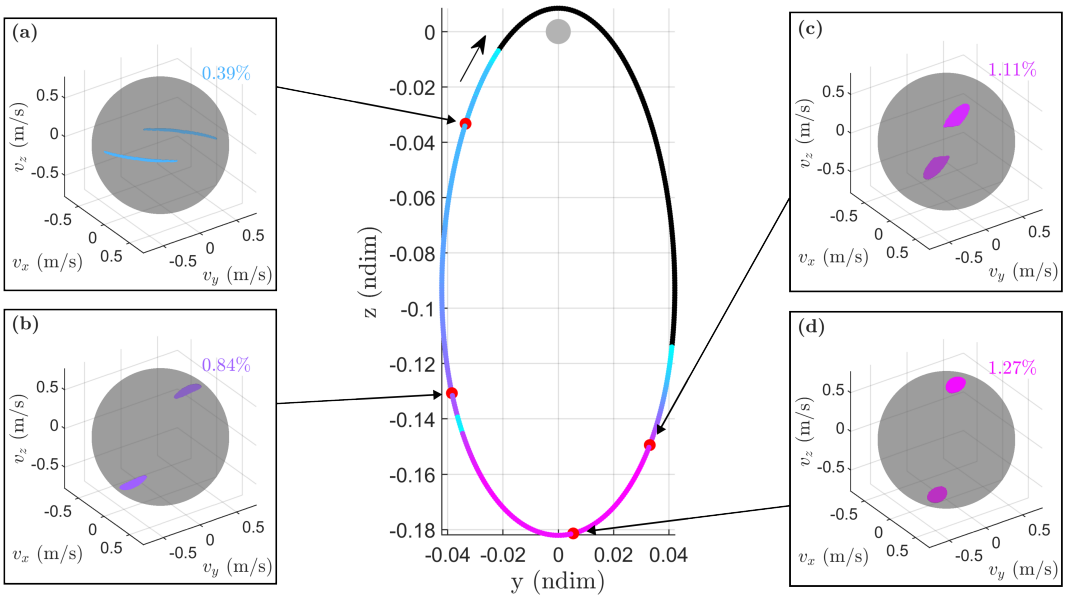

Figure 15: Feasible initial maneuver directions emerging from collision avoidance analysis for 36-hour miss time at sample NRHO locations.

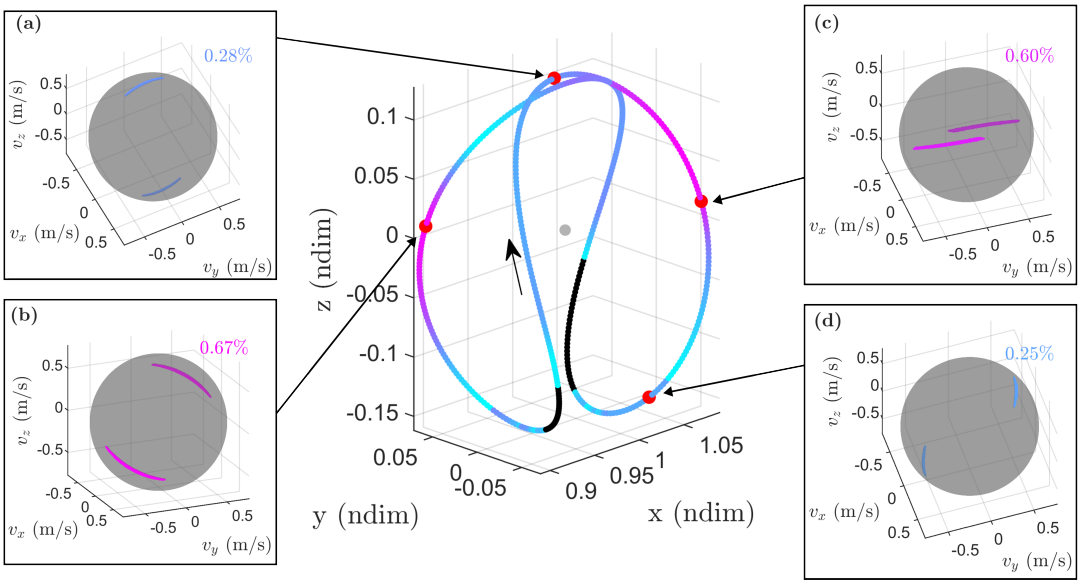

Figure 16: Feasible initial maneuver directions emerging from collision avoidance analysis for 36-hour miss time at sample butterfly orbit locations.

Accuracy of the Linear Analysis

The presented maneuver planning methodology assumes perfect state knowledge and maneuver implementation, and relies on linear dynamical simplifications evaluated along the reference orbits. To assess the accuracy of the linear predictions, sample initial conditions from the feasible maneuver directions are propagated in the CR3BP nonlinear model and the constraint compliance of the nonlinear trajectories is analyzed. For each starting location and test case, as many as 100 initial conditions are sampled from the feasible maneuvers for propagation. If fewer than 100 individual directions are identified in the linear analysis, every determined solution is evaluated. The distances from the reference path are sampled at the miss time horizon (t_{miss}) and the return time horizon (t_{return}) for each propagation and for each starting location. Summary statistics for these nonlinear distances are provided in a box-and-whisker plot, where each box-and-whisker set corresponds to the starting location on the x-axis. The box represents the inter-quartile range of the data, with a horizontal line within each box indicating the median value. The dashed lines extending above or below the box denote the upper and lower extrema and any data that exists beyond the extrema is considered an outlier, marked as individual circular points.

Data for the 24-hour miss time horizon appears in Figure 17 for the NRHO (a) and the butterfly orbit (b). For both orbits, the miss distances from the nonlinear propagation satisfy the minimum value of 100 km for all starting locations as specified. While the values are generally close to 100 km, there are regions along each reference orbit where the full range of data is well above the constraint. For the NRHO, this peaks at a starting location near 125 degrees and encompasses much of the region ahead of perilune. Along the butterfly orbit, peaks occur near 55 and 230 degrees. Recall that the velocity magnitude is determined exclusively from the miss distance and time. These regions where the values extend far beyond 100 km are locations where the maneuver magnitude may be reduced while still meeting the miss constraint.

Nonlinear compliance with the return constraint is not as consistent as the miss condition. In both orbits, there are regions where the upper extrema extend above the maximum distance of 50 km. These violations are minor along the NRHO, limited to, at most, 5 kilometers. For the butterfly, some of the extrema venture closer to 65 km. One extreme outlier dataset is observed near an encoding angle of 35 degrees along the butterfly orbit, where the full set of propagated return distances is in the 100 to 250 km range. Recall from Figure 9(a) that the return times identified for the butterfly orbit typically range from 6 to 12 days, but that a region of the orbit yields time horizons closer to 19 days. This jump in return times occurs at the same

starting locations where the inaccuracies in the linear prediction jump in Figure 17(b). The STM elements are integrated numerically along the reference trajectory from the time of the maneuver until the identified return time. As the integration time increases, the accuracy of the STM declines, resulting both from build-up of numerical error and linear inaccuracies. Thus, the correspondence between the propagated return distances and the linear prediction is quite poor in this region of the orbit where propagation times are highest.

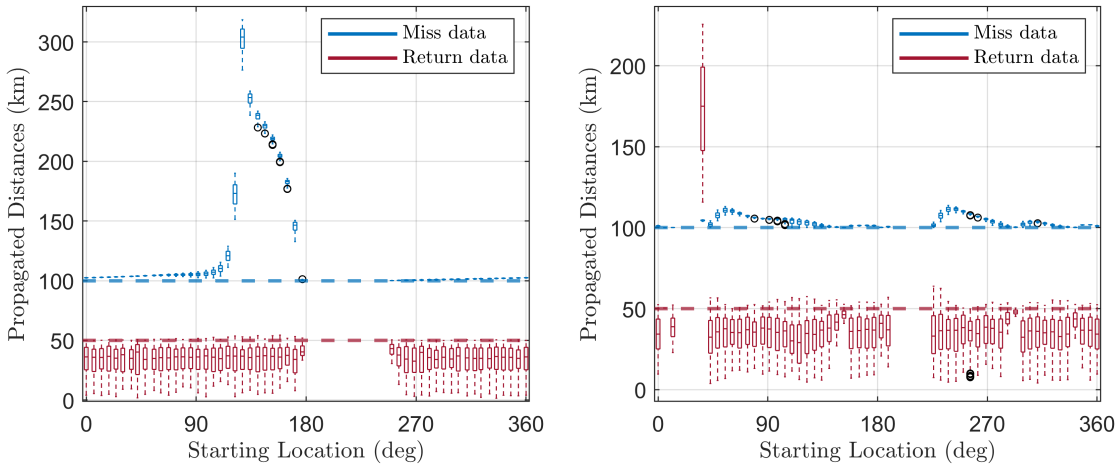

(a) Propagated distances for NRHO.

(b) Propagated distances for butterfly orbit.

Figure 17: Assessment of constraint compliance along nonlinear diverted trajectories – 24-hour miss time.

Nonlinear compliance of the miss and return constraints is assessed for the 36-hour miss time in Figure 18. Nonlinear miss distances remain entirely above the minimum bound of 100 km, with similar patterns as in the previous test case. The most significant change at this new miss time is the decrease in error for the extreme outlier associated with the butterfly orbit return condition. Distances in this outlier dataset are now entirely below 150 km. Similarly, the remaining minor constraint violations in the upper extrema for both orbits has reduced in scope, at most 54 km along the butterfly orbit and 52 km for the NRHO. The return times identified here are approximately the same as in the previous case, thus, the reduction in return distance error results from the decreased maneuver magnitude. Recall that the STM is a linearized representation of the dynamics near the reference trajectory; the linear assumptions are reasonable for sufficiently small state variations. As the maneuver magnitude grows, the resulting relative trajectories extend further from the reference path, causing the integrations to vary more from the linear prediction. The effect due to time horizon is similar, where longer integrations introduce more numerical error into both the state and STM elements.

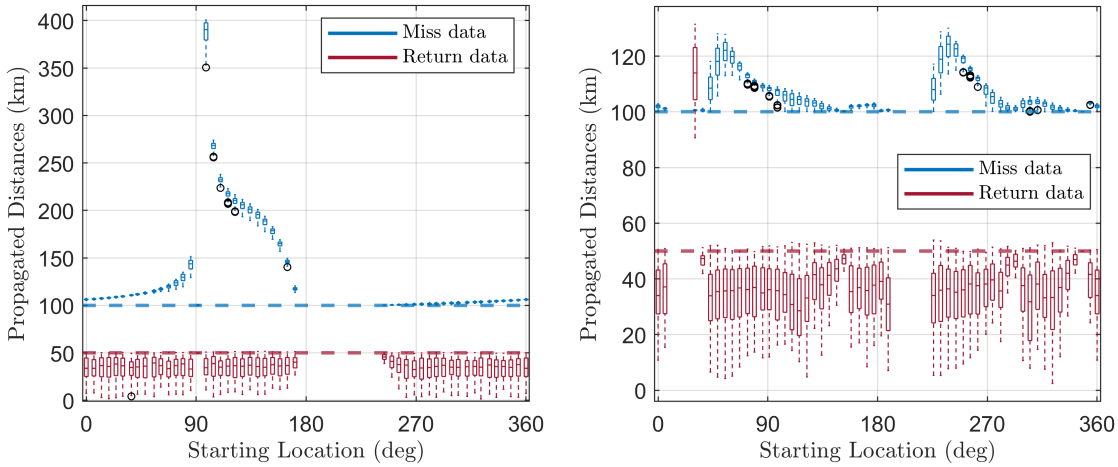

(a) Propagated distances for NRHO.

(b) Propagated distances for butterfly orbit.

Figure 18: Assessment of constraint compliance along nonlinear diverted trajectories – 36-hour miss time.

Case Study: Effect of Modifying the Constraints

To better understand the impact of the constraints on the solutions, the simulations are repeated along the 9:2 NRHO for varying values of r_{miss} and r_{return}. In each simulation, the time to conjunction is fixed at 24 hours and the maximum evaluated return time remains at 3 revolutions. Two additional values of r_{miss} are examined, increasing the minimum miss distance to 150 and 200 km for a constant value of r_{return} equal to 50 km. The percentage of CAM availability is evaluated in Figure 19(a), with data for the original 100 km value included for comparison. The availability of maneuvers scales down for each increase of r_{miss}, implying intuitively that a stricter miss condition reduces the solution space. In Figure 19(b), the maximum value of relative return velocity magnitudes at the return constraint is plotted against the starting location. There is a direct correlation between the miss distance and variational velocity magnitudes. As might be expected, increasing the minimum distance between the spacecraft and hazardous object increases the cost of the diversion.

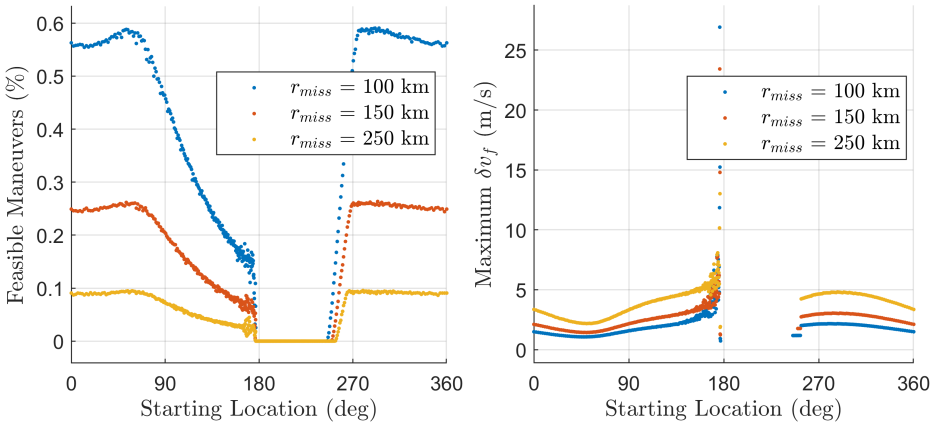

(a) Availability of maneuver directions. (b) Maximum relative return velocities.

Figure 19: Effects of varying miss distance constraint on CAM availability and final relative velocities.

Fixing the miss distance to 100 km, the return constraint is now adjusted to assess the same data. Two additional return distances are examined, tightening the constraint to 25 km and 10 km. The percentage of CAM availability appears in Figure 20(a), demonstrating similar behavior as in the miss distance study. When the constraint is tightened, the availability of maneuvers decreases, resulting directly from a decrease in the elliptic cone half angles when adjusting the r_{return} to be closer to ς_3. Figure 20(b) plots the maximum relative return velocity magnitudes for the tested return constraints. In this scenario, the return constraint does not as significantly impact the magnitudes of the final relative velocities.

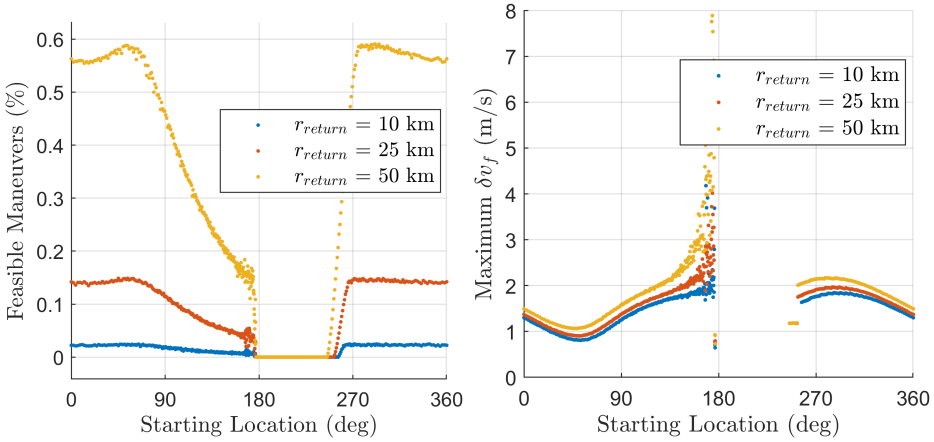

(a) Availability of maneuver directions. (b) Maximum relative return velocities.

Figure 20: Effects of varying return distance constraint on CAM availability and final relative velocities.

PRELIMINARY EVALUATION IN HFEM

A benefit of the methodology in this analysis is the dependence only on the STM, accessible directly in an ephemeris force model. Feasible maneuvers are determined in the HFEM following the same sequence of steps outlined for the CR3BP. Trajectories are propagated in a Moon-centered, J2000 reference frame, including the gravitational forces from the Sun, the Earth, and the Moon. While the true Earth-Moon distance pulsates, the equations of motion are nondimensionalized by the average characteristic quantities for numerical integration. Thus, these constant values for characteristic length and time are employed to redimensionalize the STM with Eq. (8). Figure 21 depicts twenty revolutions along a ballistic, converged NRHO in the Earth-Moon rotating-pulsating frame originating at an epoch of January 26, 2025. Consistent with the CR3BP analysis, 500 points are sampled from each revolution of the orbit and serve as initial states for the collision avoidance maneuver design, employing parameters for the 36-hour test case, i.e., 36 hours until the predicted collision. Orbit states are color-coded based on the percentage of the initial maneuver directions that meet the 100 km miss and 50 km return criteria. While results vary slightly between revolutions, the HFEM data is very similar to that from the periodic CR3BP orbit in Figure 15. Approximately the same geometric region of the orbit lacks single-CAM solutions, with similar overall availability of feasible maneuvers between the two models at corresponding orbit locations. Consistent with the CR3BP orbit, every revolution along the HFEM trajectory also produces a similar, isolated set of solutions at an earlier return time horizon, resulting in the cyan stripe following apolune. Feasible CAM options at four discrete starting locations in the HFEM trajectory are presented in Figures 21(a) through 21(d), sampled from roughly the same geometric locations as in the CR3BP orbit in Figure 15 for comparison. Available maneuvers are nearly indistinguishable between the two models. In three of the four cases, the HFEM admits a slightly increased number of CAM options than the CR3BP, on the order of a fraction of a percent. The maneuver directions and the nature of the uncovered solutions are also very similar between the models.

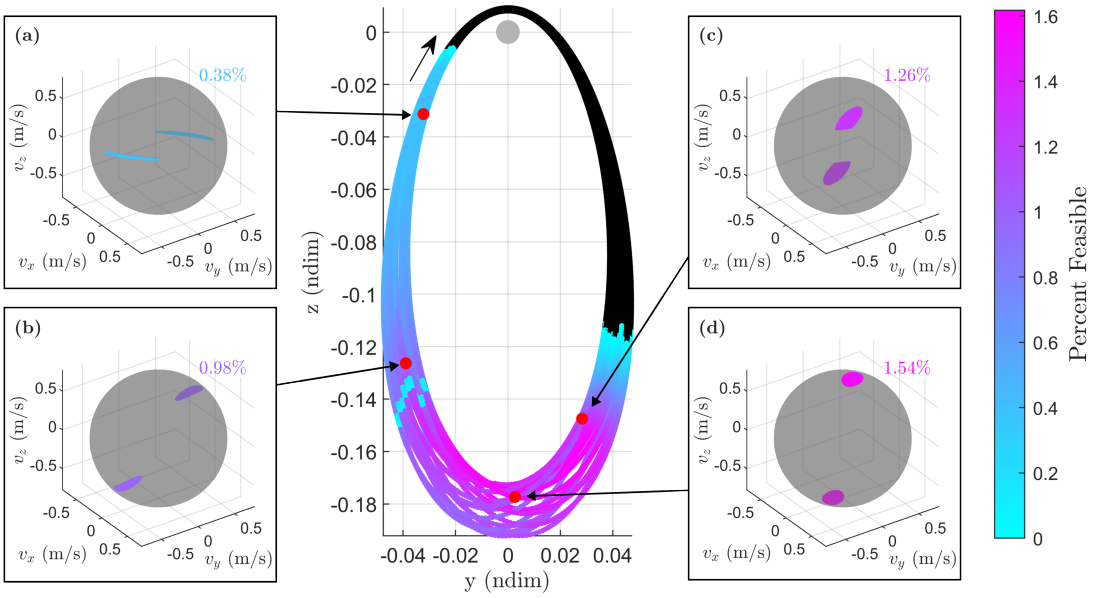

Figure 21: Feasible initial maneuver directions emerging from collision avoidance analysis for 36 hours at sample NRHO locations in HFEM.

To validate the strategy in the HFEM, feasible CAM options are applied as impulsive maneuvers to the initial trajectory state and propagated between t_0 and the identified t_{return} in the nonlinear model. For demonstration, fifty discrete maneuver directions are sampled from the feasible region in Figure 21(d) and the isochronous distances between the propagated diverted trajectories and the reference HFEM trajectory are plotted in Figure 22. The 100 km minimum safe miss distance at a time of 36 hours post-maneuver is denoted by the blue dashed lines, with the maximum return distance of 50 km denoted by the red dashed line.

Consistent with the expected behavior and CR3BP results, the nonlinear trajectories achieve the minimum miss distance at the miss time horizon, then naturally return within the prescribed upper bound at the final time. In this HFEM scenario, the trajectories pass through perilune where isochronous distances reach over 1,000 km before returning at the final time. Such a result is not surprising as isochrnous measurements include phase differences. Results in Figures 21 and 22 demonstrate the capability to leverage the presented CAM design methods directly within the higher-fidelity model.

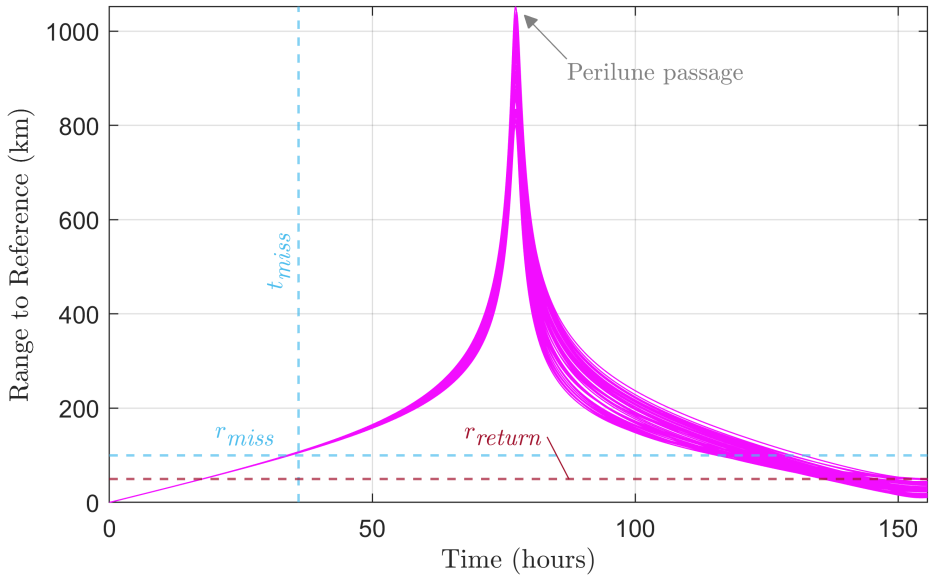

Figure 22: Demonstration of expected behavior via nonlinear HFEM propagation for maneuvers sampled from Figure 21(d).

NEXT STEPS

The current maneuver planning methodology offers opportunities for continued development. Currently, the miss condition guarantees only an isochronous separation from the reference at the time of the predicted collision, with no attention to the remaining path of the encroaching object. It is possible that the implemented trajectory diversion also endangers the spacecraft for collision at a different time, a possibility that has not yet been investigated. As mentioned previously, the minimum distance constraint is a simplification of information that results from a statistical assessment of risk probability in a true mission scenario. Incorporation of uncertainty into the spacecraft state and that of the hazardous object improves the applicability of the simulation results. Finally, while a preliminary demonstration of the methodology within the HFEM is presented here, further investigation is warranted to produce a more complete comparison of the results between the two models.

CONCLUDING REMARKS

A methodology is defined to determine impulsive maneuver options for emergency collision avoidance in multi-body orbits. The formulation leverages 3-dimensional stretching and restoring direction information, exposing the full solution space for selected constraints for a minimum safe separation distance and a maximum isochronous return distance along the diverted arcs. The strategy is evaluated on two periodic orbits in the Earth-Moon CR3BP, determining regions where a single-burn approach might be feasible for the selected constraints. Trajectory diversion options generally become more abundant when the time to predicted collision is increased, demonstrating that advanced warning time increases the flexibility in maneuver planning. As these techniques rely on linear assumptions, constraint compliance in the nonlinear model is also assessed, concluding that the return conditions are sensitive to propagation time and maneuver magnitude. A case study evaluates the effect of changing the distance constraint values. Increasing the minimum miss

distance or tightening the return constraint both reduce the availability of solutions. A larger miss distance also increases the final relative velocities, but tightening the return constraint does not have as significant of an impact on downstream velocity. Finally, the CAM design methods are applied directly in a HFEM to highlight the independence of the approach to the dynamical model selected. A primary benefit of this effort is gaining insight into natural motion as a starting point for more in-depth analysis and mission applications.

ACKNOWLEDGMENTS

This work was supported by a NASA Space Technology Graduate Research Opportunity, NASA grant number 80NSSC24K1364. The authors also wish to acknowledge Purdue Ph.D. student Mitchell Dominguez for his assistance with the HFEM demonstrations in this investigation.

REFERENCES

[1] H. Cowardin and A. Johnson, "Orbital Debris Quarterly News, National Aeronautics and Space Administration," Vol. 26, December 2022.

[2] E. Zimovan, K. C. Howell, and D. C. Davis, "Near Rectilinear Halo Orbits and Their Application in Cis-Lunar Space," *3rd IAA Conference on Dynamics and Control of Space Systems*, Moscow, Russia, May-June 2017.

[3] S. Dutta and A. K. Misra, "Convex optimization of collision avoidance maneuvers in the presence of uncertainty," *Acta Astronautica*, Vol. 197, 2022, pp. 257–268.

[4] J. Hernando-Ayuso and C. Bombardelli, "Low-Thrust Collision Avoidance in Circular Orbits," *Journal of Guidance, Control, and Dynamics*, Vol. 44, No. 5, 2021, pp. 983–995.

[5] J. Mueller, "Onboard Planning of Collision Avoidance Maneuvers Using Robust Optimization," *AIAA Infotech@Aerospace Conference*, Seattle, Washington, April, 2009.

[6] L. De Maria, A. De Vittori, and P. Di Lizia, "Numerically Efficient Impulsive and Low-Thrust Collision Avoidance Manoeuvres in Cislunar L1-Near Rectilinear Halo Orbit," *74th International Astronautical Congress (IAC)*, Baku, Azerbaijan, October, 2023.

[7] Z. Pavanello, L. Pirovano, and R. Armellin, "Recursive Polynomial Method for Fast Collision Avoidance Maneuver Design," *IEEE Transactions on Aerospace and Electronic Systems*, (Preprint), June, 2024, pp. 1–12.

[8] D. C. Davis, E. M. Zimovan-Spreen, S. T. Scheuerle, and K. C. Howell, "Debris Avoidance and Phase Change Maneuvers in Near Rectilinear Halo Orbits," *44th Annual AAS Guidance, Navigation, and Control Conference*, Breckenridge, Colorado, February, 2022.

[9] L. Nugent, "Stretching and Restoring Directions as a Basis for Relative Trajectory Design," M.S. Thesis, Purdue University, West Lafayette, Indiana, 2024.

[10] "The Navigation and Ancilliary Information Facility - NASA JPL," October, 2024. `https://naif.jpl.nasa.gov/naif/`.

[11] L. Nugent and K. Howell, "Relative Trajectory Design Methodologies Informed by Stretching and Restoring Directions," *AAS/AIAA Astrodynamics Specialist Conference*, Broomfield, Colorado, August, 2024.

[12] E. M. Zimovan-Spreen, K. C. Howell, and D. C. Davis, "Near rectilinear halo orbits and nearby higher-period dynamical structures: orbital stability and resonance properties," *Celestial Mechanics and Dynamical Astronomy*, Vol. 132, Jun 2020, p. 28.

[13] K. Chan, "Collision Probability for a General Spacecraft," *American Astronautical Society Conference*, Charlotte, Virginia, February, 2021.

[14] D. A. P. Williams, K. C. Howell, and D. C. Davis, "Dynamics Leveraged in Long-Term Stationkeeping Strategies for Multi-Body Orbits," *AAS/AIAA Astrodynamics Specialist Conference*, Broomfield, Colorado, August, 2024.